Anomalous temperature dependence of yield strength and deformation mechanisms in chemically complex intermetallic alloy

Jinxiong Hou[a, b1*], Jie Gan[b1], Tao Wang[a*], Zhongkai Ren[a], Junhua Luan[b], Zhixiong Zhang[a], Tuanwei Zhang[c], Wei Wen[d], Zhihua Wang[a, c*], Tao Yang[b]

[a] *College of Mechanical Engineering, Taiyuan University of Technology, Taiyuan, Shanxi Province 030024, China*

[b] *Department of Materials Science and Engineering, City University of Hong Kong, Tat Chee Avenue, Kowloon Tong, Kowloon, China*

[c] *College of Aeronautics and Astronautics, Taiyuan University of Technology, Taiyuan, Shanxi Province 030024, China*

[d] *School of Engineering, Lancaster University, Lancaster, LA1 4YW United Kingdom*

[1] *Those authors contribute equally to this work*

*Corresponding author at: jxhou@tyut.edu.cn; twang@tyut.deu.cn; zhihuawang@tyut.edu.cn

Abstract

A chemically complex intermetallic alloy (CCIMA) dominated with an ordered $L1_2$ structure was designed based on the multicomponent Ni-Co-Cr-Al-Mo-Ti-Ta-Nb-B system. Its phase structure, mechanical behaviors, and underlying deformation mechanisms were investigated systematically at room and elevated temperatures. The CCIMA yields at a strength of 758 ± 2 MPa at room temperature, maintaining a pronounced work-hardening rate of ~ 4530 ± 10 MPa throughout the entire deformation, which achieves an ultimate strength of ~ 1490 ± 12 MPa attributing to the formation of anti-phase boundary (APB) together with superlattice intrinsic stacking fault (SISF). A remarkable temperature-dependent anomaly in yield strength

is formed at temperatures below about 800 ℃, obtaining a high increase of strength for nearly 200 MPa relative to that at 20 ℃. Such yield strength anomaly (YSA) is caused by the pinning of Kear-Wilsdorf (K-W) locks, which results from thermally activated superlattice dislocations moving from the (111) octahedral plane to the (010) cube plane. Furthermore, a transition of dissociation scheme from APB-type at intermediate temperatures to SISF-type at 900 ℃ is believed to be responsible for the absence of YSA at higher temperatures. The CCIMA shows a high strength and peak of flow stress around 800 °C, signifying a great potential for elevated temperatures applications.

Keywords: Intermetallic alloys; Microstructures; Yield strength anomaly; Deformation mechanisms.

1. Introduction

As a new class of potential high-temperature structural materials, more and more extensive efforts have been dedicated to developing intermetallic alloys derived from the principal hexagonal close-packed (HCP), body-centered-cubic (BCC), and face-centered-cubic (FCC) structures [1, 2]. In the ordered intermetallics, the designated lattice sites are occupied with specific atomic species, by which a strong chemical bonding between elements is established, thereby yielding exceptional retention in relation to their modulus and strength at high temperatures [2]. HCP lattice-based $D0_{19}$-type Ti_3A1 intermetallic compoundsshow low density and high strength, have received attention in applications at elevated temperatures their low density and high strength make them attractive, However, they are unsuitable for use above

600 °C owing to a rapid decrease of strength [3]. Likewise, the yield strength of BCC lattice-based intermetallic compounds such as NiAl, FeAl, and CoAl decreases rapidly due to the fast diffusion process above 0.6 T_m [1]. To date, the FCC lattice-based Ni_3Al and relevant intermetallic compounds have gained the greatest amount of scientific attention, mainly attributing to the technological importance of the strengthening phase in Ni-based superalloys and a remarkable yield strength anomaly (YSA) behavior at elevated temperatures. For example, Ni_3Al presents YSA at temperatures varying below 0.5 T_m while the Co_3(Al, W) has a much wider YSA regime below 0.63 T_m [4, 5]. It is worth mentioning that the severe grain boundary embrittlement in polycrystalline Ni_3Al intermetallics can be effectively mitigated by microalloying with boron [6], benefits from which the boron-dopped off-stoichiometric Ni_3Al alloy obtained a more than 40% plastic strain to failure with a fully transgranular fracture [7-9]. Consequently, the ductilization of polycrystals Ni_3Al-based intermetallics has largely focused on the controllable alloying with boron in off-stoichiometric intermetallics.

Based on the concept of boron-doped off-stoichiometric composition design, recently a creative alloying concept that has largely substituted the lattice sites with multiple elements aids the design of a series of chemically complex intermetallic alloy (CCIMA) with excellent ductility and strength derived from Ni_3Al [8, 10-13]. By substituting the Al-sublattice with elements (like Ti, Zr, Nb, Ta, Re, Cr, Mo, W, V, Hf), the anti-phase boundary energy (APBE) of the Ni_3Al can be increased accordingly, thereby improving their strength at both room and elevated temperatures [14-17]. Moreover, alloying with specific elements can shift the peak temperature of YSA. For instance, the addition of Cr, Ti, or their combination (10.5 at.% Ti + 2 at.% Cr) can essentially raise the peak temperature relative to Ni_3A1 by nearly 150 °C,

whereas the peak temperature is decreased by 50 °C with a 6 at.% addition of Nb [18]. Hence, the synergistic alloying effects with multiple elements and their substitution can not only enhance the strength but also control the YSA behavior in the CCIMA.

Generally, $L1_2$-type ordered alloys such as Ni_3Al, Ni_3Si, Ni_3Ge, and Zr_3Al behave an astonishing YSA at elevated temperatures, which may be caused by thermally activated cross-slip of these anti-phase boundary (APB)-coupled dislocations from the (111) octahedral to (010) cube planes [19-22]. Alternatively, there exist some other $L1_2$ intermetallic compounds, like Pt_3Al, Pt_3Ga, and Pt_3In, which show either no distinct peak or a slight peak of the flow stress at high temperatures despite the dissociation scheme is of the APB-type [23]. Additionally, similar to conventional FCC metals, the absence of the YSA at high temperatures is found in $L1_2$-type Fe_3Ge, Ir_3Ti, and Ir_3Nb [1, 24]. In strong contrast, Yamabe-Mitarai [25] reported that the dissociation scheme of the superlattice intrinsic stacking fault (SISF)-type, as revealed by TEM analysis, is taken as a new mechanism response for the YSA of $L1_2$-type Ir_3Nb. In conclusion, the occurrence and absence of YSA behavior in $L1_2$-type are strongly dependent on the types of intermetallic alloy, and the YSA behavior is closely linked to their dislocation dissociation during the deformation, which has not yet been well understood in CCIMA.

Based on the analysis above, boron was introduced to a ductile alloy system with off-stoichiometric compositions. Multicomponent alloying like Mo, Ti, Ta, and Nb allow for strengthening the alloy at both room and elevated temperatures towards a higher peak regime of YSA. This study delved into the phase structure and tensile behaviors of CCIMA from 20 to 1000°C. The temperature-dependent deformation mechanisms, where the different dislocation dissociation governs, are also uncovered. Furthermore, the relevant YSA mechanisms were

studied in light of the dislocation dissociation scheme on (001) and (111) planes at both room and elevated temperatures.

2. Experimental

The novel chemically complex intermetallic alloy (CCIMA) with a nominal composition of $Ni_{33}Co_{39}Cr_5Al_{12}Mo_2Ti_3Ta_2Nb_3B_1$ (at.%) was arc-melted under an Argon atmosphere in a water-cooled copper crucible. To ensure chemical homogeneity, each ingot button was melted, flipped, and re-melted at least eight times and then cast into a copper mold with a cavity of 35× 15 × 3.5 mm^3. The ingots were annealed at 1100 °C for 2 h and then cold rolled to approximately 1.5 mm in thickness by a repeated rolling method (~ 15% reduction in thickness per step) at room temperature, with intermediate annealing at 1100 °C for 15 min. Finally, the rolled sheets were recrystallized at 1100 °C for 30 min. The microstructures were examined using scanning electron microscopy (SEM, Quanta FEG450) equipped with electron backscatter diffraction (EBSD, velocity) and transmission electron microscopy (TEM, JEM-2100F) equipped with energy dispersive X-ray spectrometry (EDS). 3D Atom probe tomography (3D-APT, LEAP 5000XR) was also employed to determine the bulk chemical compositions. Dog-bone-shaped tensile samples with a gauge length of 12.5 mm and a width of 3.2 mm were performed at a strain rate of 10^{-3} s^{-1} in the temperature range of 20 to 1000 °C.

Commented [WW1]: 这个是从哪个方向轧的？可以写 thickness 从 35， 15，或者 3.5 压成的 1.5。

Commented [WW2]: 这个实在什么时候进行的？是每次轧制中间吗？作用是啥？需要说明一下

3. Results

3.1 Microstructures

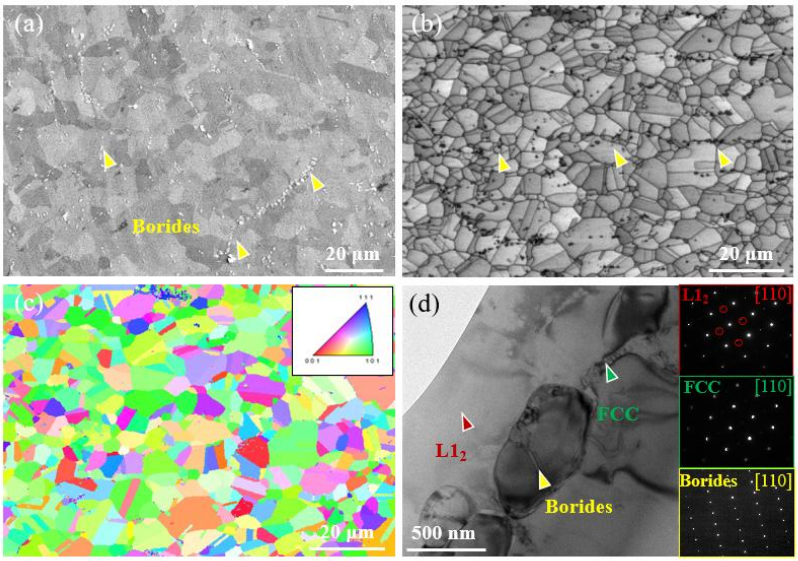

Fig. 1 (a) SEM image of the CCIMA showing the distribution of borides. (b) EBSD band contrast map and (c) inverse pole figure of the present CCIMA. (d) Bright-field TEM image of the CCIMA showing the constitutes phases, the inserted selected area electron diffraction (SAED) patterns correspond to the marked phase.

Figure 1a shows the SEM image of the as-prepared CCIMA samples, with small borides can be seen. The EBSD band contrast map and inverse pole map in **Figs. 1b** and **c** reveal that the CCIMA is in a fully recrystallized state, with an average grain size of 5.0 ± 1.7 μm. The structure features can be obtained from the TEM analysis, involving the bright image and related selected area electron diffraction (SAED) patterns in **Fig. 1d**, where the superlattice

spots demonstrate that the dominant phase has an $L1_2$ structure. There exist FCC phase and borides within the $L1_2$ phase, the FCC phase has a coherent relationship with the $L1_2$ phase, while the borides can be indexed with a Re_3B structure from the SAED pattern in the inserted image [13].

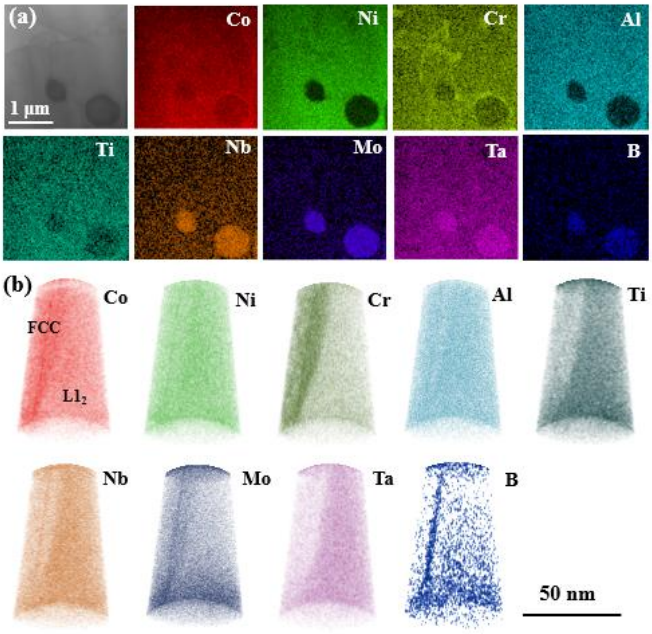

Fig. 2 (a) Scanning transmission electron microscope (STEM) and corresponding EDS images of the present CCIMA. (b) 3D reconstructions of a typical APT tip showing the elemental partitioning between the $L1_2$ phase and the FCC phase.

The STEM image and associated EDS maps of the CCIMA are given in **Fig. 2a**, the FCC phase is enriched with Ni, Co, and Cr elements, and the borides are enriched with Co, Nb, Mo, Ta, and B from the STEM image. By employing a more detailed view from the 3D-APT reconstructions in **Fig. 2b**, the $L1_2$ phase is confirmed as a multi-component $(Ni, Co)_3(Al, Ti,$

Nb, Ta)-type phase. Mo seems to have a relatively high content in the FCC phase, the enrichments of Ni, Co, and Cr in the FCC phase can be further confirmed from the APT analysis. By adjusting the iso-composition surfaces of B, significantly, a co-segregation of B, Co, Ni, Cr, Mo, and Nb can be found at the interface between the FCC and $L1_2$ phases.

To quantify the constitute elements between the FCC and $L1_2$ phase, a compositional profile across the phase interface along the cylinder in **Fig. 3a** is given in **Fig. 3b**, from which the detailed contents of the constitute elements can be statistically shown for each phase. A magnification rectangle region shows the interfacial segregations of Co, Cr, Nb, Ta, and B in the present alloy, which is similar to a disorder FCC layer at the boundaries [8].

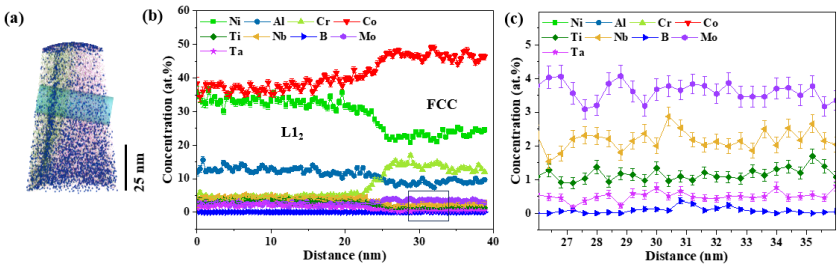

Fig. 3 (a) 3D reconstructions of a typical APT tip superposed with B and Nb with a cylinder across interface of FCC and $L1_2$ phases. (b) Atomic concentration of individual elements across the interfaces and (c) a magnified atomic concentration with low contents.

Commented [WW3]: 在 b 里 interface 可以用虚线标一下。图 a 里可以画个箭头标一下 distance 是从哪到哪

3.2 Mechanical properties

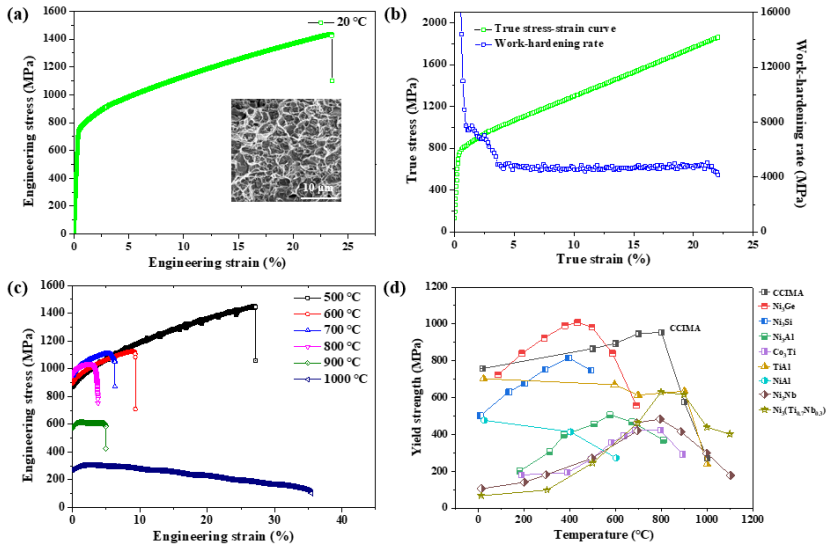

Fig. 4 (a) Stress-strain curve and (b) work-hardening rate of the CCIMA at 20 °C. (c) Stress-strain curves of the CCIMA at elevated temperatures. (d) Temperature dependence of yield stress in the CCIMA and other ordered alloys. The insert in (a) shows the fractured surface with abundant dimples.

Commented [WW4]: 图 c 是不是直接方 true stress true strain curve 好一些?

Commented [WW5]: 文献里来的数据需要引用一下

As given in **Fig. 4a**, a superior synergy of strength and ductility is obtained in the present CCIMA at room temperature (20 °C), and a natural ductile failure with abundant dimples is found from the inserted fracture morphology. The CCIMA starts to yield at a strength of 758 ± 2 MPa, achieving an ultimate strength of ~ 1490 ± 12 MPa after straining for an elongation of ~ 23.4%. As shown in **Fig. 4b**, a pronounced work-hardening rate with a high value of ~ 4530 ± 10 MPa can be sustained until failure, indicating the exceptional work-hardening rate in the

CCIMA. Attributing to this expectational work-hardening rate, a high ultimate strength close to twice the yield strength is obtained in the CCIMA, which has been confirmed when compared to the classic disorder alloys [26].

Fig. 4c displays the tensile stress-strain curves at elevated temperatures. The CCIMA presents a high strength and ductility synergy when deformed at 500 ℃. However, the fracture strain rapidly decreases to ~ 9% at 600 ℃, and further reduces to ~ 3% at 800 ℃ due to the intermediate temperature embrittlement [27]. Interestingly, an anomalous increase in yield stress is observed at temperatures below 800 ℃ despite severe oxygen-induced embrittlement occurring, as a consequence, the alloy tends to yield at a high strength of ~ 947 ± 12 MPa at 800 ℃. At 900 ℃, the yield strength of CCIMA suddenly decreases to 575 ± 15 MPa, and the ductility is recovered to ~ 5%. At 1000 ℃, a low yield strength of 270 ± 12 MPa together with a high elongation of ~ 35% is found in the CCIMA. **Fig. 4d** compares the temperature dependence of the yield stress among the $L1_2$-type Ni_3Al, Ni_3Ge, Ni_3Si, and Co_3Ti [28, 29], B2-type NiAl [30], $D0_{19}$-type $Ni_3(Ti_{0.7}Nb_{0.3})$ [31], D0a-type Ni_3Nb [32], polysynthetic twinned TiAl [33] and the present CCIMA, from which the CCIMA has a relatively high yield strength at temperatures from 600 to 800 ℃. In addition, the CCIMA shows a high peak of flow stress around 800 °C, with a higher peak temperature relative to Ni_3A1 by nearly 100 °C, thereby signifying a great potential for elevated temperatures applications.

3.3 Deformation microstructures at room temperature

To reveal the dislocations structures at room temperature, TEM images under a two-beam condition with electron beam direction along [011] are shown in **Fig. 5**. Low-density

superlattice dislocations dominate the deformation in an inhomogeneous distribution manner at a strain of 5% in **Fig. 5a**, where the curved and planar superlattice dislocations together with loop-like configurations can be seen. The curved dislocations suggest the frequent occurrence of cross-slip from one of the octahedral slip planes to another octahedral slip plane [34], as in the case of FCC metals [35]. When the moving superlattice dislocations encounter the FCC phase, They extend into the FCC region but terminate at the adjacent $L1_2$ phase in **Fig. 5b**. A close-up view in **Fig. 5c** shows that the dislocations are primarily impeded by the borides, and no measurable crystallographic defects are formed inside the borides. Note that, no superlattice intrinsic stacking fault (SISF) is found at a low strain of 5% in the $L1_2$ phase, which is similar to the boron-dopped Ni_3Al-based intermetallic compound where alloying with boron lowers the APB energy, thereby suppressing the formation of SISF in the Ni_3Al alloy [36].

With the tensile deformation further proceeding to ~ 25%, massive dislocations in the vicinity of the GBs and the ordered grain interiors are formed, and their complex interactions result in the dislocation tangles in the $L1_2$ phase in **Fig. 5d.** High-density dislocations can accumulate in the $L1_2$ phase around the boride as shown in **Fig. 5e.** Similarly, the crystallographic defects in borides cannot be observed even under such a high strength level. The presence of the planar-type SISFs can be found in the CCIMA at a high strain of ~ 25% from **Figs. 5f** and **g**. As magnified in the HRTEM image in **Figs. 5h** and **i**, the nano-spaced SISF networks are formed, known as L-C lock, which can suppress their further prorogations. Therefore, both the superlattice dislocations and the SISF networks could contribute to the expectational work-hardening rate by dragging on super dislocations as their formation.

Commented [WW6]: 我个人感觉光凭 curved 不能说明 cross slip 很频繁。但如果你们可以确定就不用动。

Commented [WW7]: 这句话我没看懂。

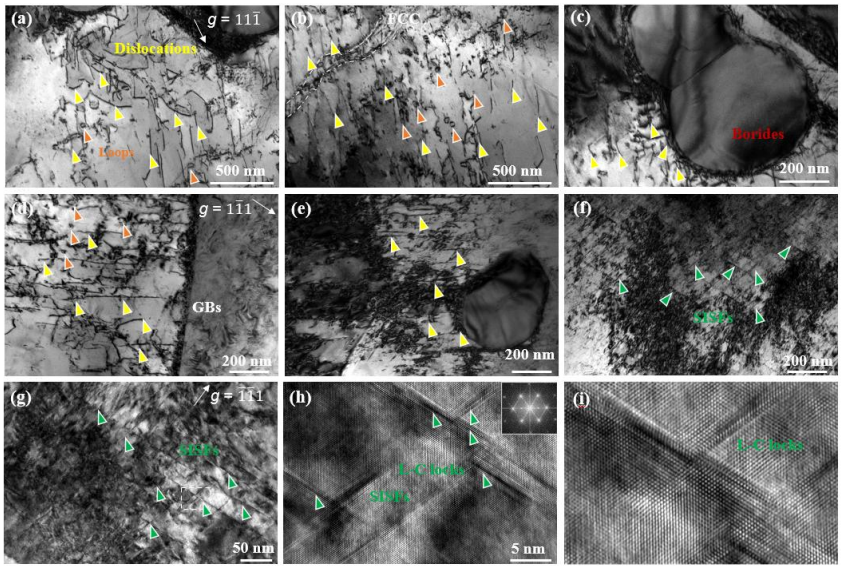

Fig. 5 TEM images in the CCIMA tensile specimen after 5% strain at RT, showing dislocation activities at (a) $L1_2$ phase region, (b) $L1_2$ + FCC region, and (c) $L1_2$ + borides region. TEM images in the CCIMA tensile specimen after 25% strain at RT, showing dislocation activities at (d) vicinity of GBs and $L1_2$ phase region and (e) $L1_2$ + borides region. (f) Formation of SISFs and (g) magnified SISFs with nano-spaced networks. (h) HRTEM image of SISF networks with L-C lock configurations. All the TEM images were taken close to [110] zone axial with different g vectors.

3.4 Deformation microstructures at elevated temperatures

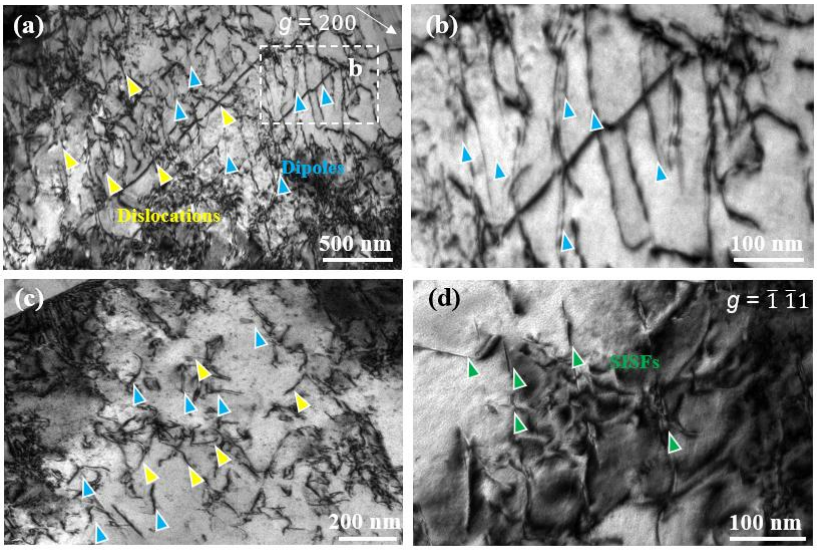

Fig. 6 TEM images in the $L1_2$ phase region after fracture at 700 °C, showing (a) dislocations and dislocation dipoles and (b) magnified image. TEM images in the $L1_2$ phase region after fracture at 800 °C showing (c) dislocation dipoles and (d) SISFs. All the TEM images were taken close to [110] zone axial with different g vectors.

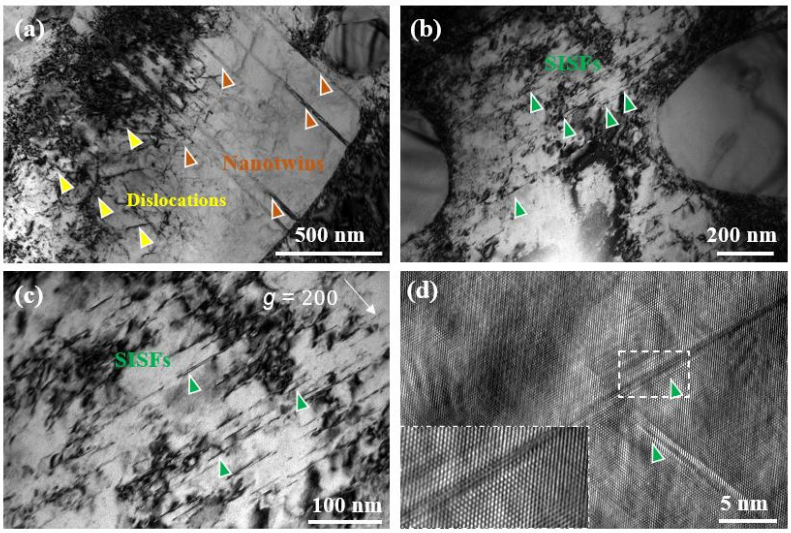

Fig. 7 TEM images in the $L1_2$ phase region after fracture at 900 °C. (a) Dislocations and nano twins, (b) SISFs and magnified dislocations dipoles and its enlarged (c) dark field image, and (d) dislocations in borides. All the TEM images were taken close to [110] zone axial with different g vectors.

Figure 6a shows the dislocation structures deformed at 700 °C, where super dislocations travel in a cross-slip configuration in ordered lattices, dislocation dipoles with collinear super partial dislocations are magnified in **Fig. 6b**. When the deformation temperature rises to 800 °C, short dislocation dipoles are observed which lie on the (111) slip plane, indicating the deformation temperature is high enough for significantdislocation climb . In addition to the paired traveling superlattice dislocations in **Fig. 6c**, the appearance of the SISFs occurs in **Fig. 6d**. When the temperature rises to 900 °C, in strong contrast, the nanotwins and SISFs generate in **Figs. 7a** and **b**, respectively. A further magnified image and HRTEM image in **Figs. 7c** and

d show the formation of SISFs, the inset in **Fig. 7d** shows the SISF. Collectively, the temperature-dependent deformation structures can be concluded as: (i) the increase in the cross-slip segments at 700 °C; (ii) in addition to the dislocations, the appearance of the SISFs at 800 °C occurred, and the enhanced SISFs even in the form of nano twins can be seen at 900 °C in the CCIMA.

4. Discussion

4.1 Dislocation structures change accounts for the anomalous yield strength

Since the widely accepted theory for YSA involves a transformation of the screw dislocation core from a glissile form into a sessile form. The dislocation structures change can be observed when comparing the results at 20 and 700 °C. As shown in **Figs. 8a** and **b**, the dislocations with two collinear super partials separated by an APB are found at 20 °C. By changing the diffraction conditions in **Figs. 8c**, **d**, **e,** and **f**, the Burger vectors of the involved dislocations can be deduced based on the validation through the $g \cdot (b \times u)$ criterion [37]. A Burger vector for dislocation type A (marked by red arrows) can be confirmed as $b = \pm 1/2[\bar{1}10]$ because of the invisible type A dislocations at a diffraction condition of $g = [220]$. Moreover, type A dislocation lines are parallel to the g vector of $[\bar{2}20]$, confirming the screw character of those dislocations. Following the logic above, we can find that the type B dislocations are accompanied by a Burger vector of $b = \pm 1/2[\bar{1}10]$. A two-fold dissociation characteristic is observed along the dislocations imaged in **Figs. 8e** and **f** under reflection vectors of $[220]$ and $[\bar{2}20]$, respectively. By imaging the marked dislocation in **Fig. 8f** under a g(3g) diffraction condition, the separation of the APB-coupled unit dislocations is measured

as 2.7 nm in **Fig. 8e**. Therefore, there exist screw dipoles in the CCIMA when deformed at room temperature.

When the deformation temperature increases to 700 °C, as displayed in **Figs. 9a** and **b**, more complicated dislocation interactions among the dislocation dipoles occurred. Based on the $g \cdot (b \times u)$ criterion and various diffraction conditions in **Figs. 9c-f**, the Burgers vector of type A dislocations (marked by red arrows) is $b = \pm 1/2[\bar{1}10]$. Additionally, the dislocation lines of type A are primarily parallel to $g = [\bar{2}20]$, confirming the screw character of those dislocations. In many $L1_2$ compounds, the separation distance for the coupled superpartials is observed to be the widest along the [010] zone-axis [38, 39]. Specifically, the widest spacing between the dislocation pairs in **Fig. 9g** become narrow even almost undiscernible, meaning that those segments undergo a cube cross slip. In addition, those long-segment dislocations marked by red arrows in **Figs. 9a** and **b** demonstrate 60° mixed character compared to short segments marked by green arrows, suggesting the cross-slip process from the octahedral plane onto the cube plane [40]. The cross-slip of screw dislocations onto cube planes is a common behavior for super dislocations, which is often referred to as Kear-Wilsdorf (K-W) locks [41, 42]. As such, the YSA behavior becomes remarkable at intermediate temperatures, where mostly screw dipoles can be observed in the deformed samples in **Fig. 9**. Assuming the marked dislocation in **Fig. 9** is under a g(3g) diffraction condition, the separation of the APB-coupled unit dislocations is measured as 5.7 nm in **Fig. 9e**.

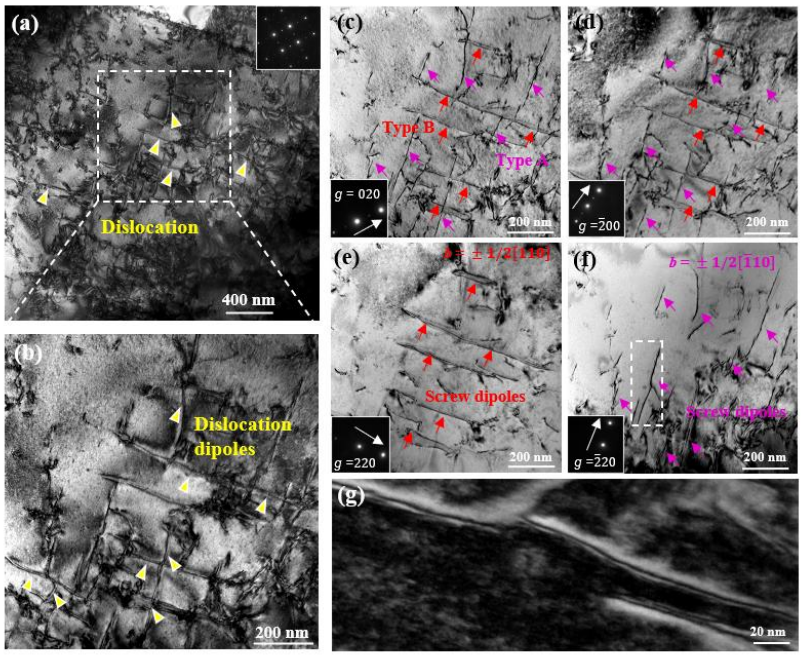

Fig. 8 TEM images in the $L1_2$ phase region of the sample fractured at 20 °C along [100] zone axial and under various g vectors. (a) and (b) along [100] zone axial. (c) g = [020], near [100]. (d) g = [$\bar{2}$00], near [100]; (e) g = [220], near [100]; (f) g= [$\bar{2}$20], near [100]. (g) Weak-beam image of dissociated dislocations observed along [100] at g= [$\bar{2}$20], g/3g condition in (f).

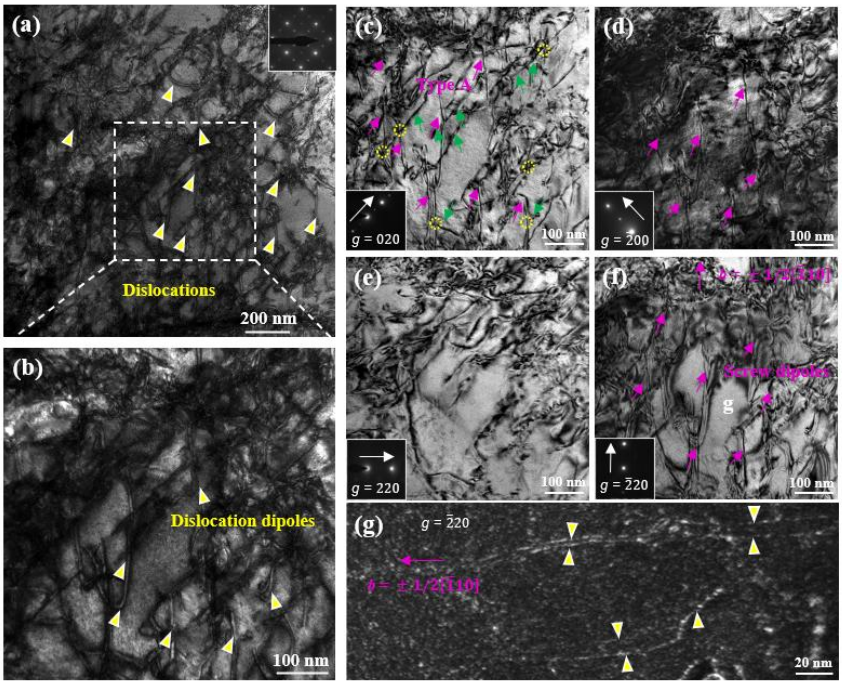

Fig. 9 TEM images in the $L1_2$ phase region of the sample fractured at 700 °C along [100] zone axial and under various g vectors. (a) and (b) along [100] zone axial. (c) g = [020], near [100]. (d) g = [$\bar{2}$00], near [100]; (e) g = [220], near [100]; (f) g= [$\bar{2}$20], near [100]. (g) Weak-beam image of dissociated dislocations observed along [100] at g= [$\bar{2}$20], g/3g condition.

At intermediate temperatures, the moving {110} superlattice screw dislocations can cross slip from octahedral {111} onto cube {001} due to the anisotropy in the APB energy on the {111} and {100} planes in Ni_3Al [18] and Ni_3(AI, W) [43] intermetallic compounds. The experimental evidence of pinning points along screw dislocation segments can be seen in **Figs. 9a** and **b**. As schematically shown in **Figs. 10a** and **b**, the dislocation is dissociated into two $1/2[\bar{1}01]$ superpartials bounding an APB which lies partly on (111) and and (010) [44].

The {001} slip planes become preferred slip planes when the thermally activatedmotion of sessile screw dislocations is preferred on these planes. These cross-slipped segments of screw dislocation act as pinning points for the entire dislocation motion [5] [45], forming the immobile K-W locks on the initial (111) upon the stress [46]. According to atomistic studies by Yamaguchi et al. [47] and Paidar et al. [48], dislocations become sessile on {001} plane, i.e., the cores of <110> superlattice screw dislocation on the {001} plane never spread onto the {001} plane and exhibit a sessile configuration which spreads onto the (111) or (1-11) plane.

As well noted from the references, it is the anisotropy in APB energy that gives a driving force for the dislocation climb from the octahedral {111} onto cube {001} with the condition that $\lambda = \gamma_{100}/\gamma_{111} < 1/\sqrt{3}$ based on the Paidar, Pope, and Vitek (PPV) model [5]. Yoo further modified the condition by combining the anisotropy of the APB energy and the elastic interaction force as [35]:

$$\lambda = \gamma_{100}/\gamma_{111} < 1/(\sqrt{3}/(1 + f\sqrt{2}) \quad (1)$$

$$f = \sqrt{2}(A - 1)/(A + 2) \quad (2)$$

where A is a material parameter depending on the elastic shear constants $A = 2c_{44}/(c_{11} - c_{12})$, with c_{12}, c_{44} and c_{12} are elastic constants. This modified condition from the above equation can favor the glide plane (111) onto the cross-slip plane (001) arising from the anisotropic torque term. The above modification is based on the condition that the dislocation pair experiences a positive force, initially loading on the (111) plane and then driving the pair onto the (010) cross-slip plane. If the initial cross-slip driving force is negative, Saada and Veyssiee`re [49] showcased a method that calculates the energy rather than the force, which allows the dissociation on the (010) plane to be favored energetically over that on the (111)

plane even with a negative force. For this latter criterion, an energy-based condition is described by:

$$\lambda < 3^{1/4}B^{1/2} \tag{3}$$

$$B = 3^{1/2}\mathrm{A}/(\mathrm{A}+2) \tag{4}$$

Based on the above argument on the condition for cross-slip, as shown in **Fig. 10c**, a 'map' can be constructed based on the two material parameters λ and A. Thus, with the increase in Zener anisotropy, the YSA can be derived despite that the APB energy difference in the two planes is decreased [44].

Commented [WW8]: 没有 10c。。。

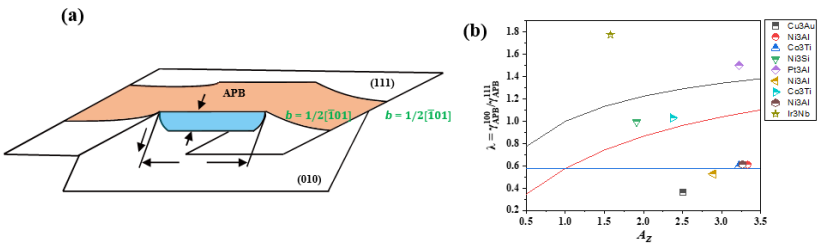

Fig. 10 (a) A schematic drawing of the cross-slip of one super partial from the (111) to the (010) plane by the double kink mechanism. (b) The $\lambda - A$ map showing the various necessary condition for the yield stress anomaly.

For the presentCCIMA alloy, the alloying effect of solute substitution at the sublattice site of the Ni_3Al phase on APB energy can be quantified through Eq. 5 [17, 50]. In this work, we assume that the relationship between the APB energy and the composition is linear, and consequently, one has:

$$\gamma_{APB} = \gamma_{APB}^{0} + 136.0 \cdot C_{Co}^{\gamma'} + 239.6 \cdot C_{Cr}^{\gamma'} + 269.0 \cdot C_{Mo}^{\gamma'} + 270.5 \cdot C_{Ta}^{\gamma'} + 232.3 \cdot C_{Ti}^{\gamma'} + 226.8 \cdot C_{Nb}^{\gamma'} \tag{5}$$

Taking $\gamma_{APB}^{0} = 182.0$ mJ/m^2, and the γ_{APB}^{111} in present CCIMA can be assumed as 273.4 mJ/m^2 on the consideration of the alloy effects. It has been pointed out that the K-W mechanism is responsible to the occurrence of YSA. Therefore, according to the energy relationship from the map in **Fig. 10c**, the $\gamma_{\mathrm{APB}}^{100}$ has an upper bound ranging from 157.8 to 292.5, and then to 371.84 mJ/m^2 when considering the above three criterions. Here, A is borrowed from the Ni_3Al alloy as 3.27 [51]. As given in **Fig. 10c**, it is clear that the Pt_3Al and Ir_3Nb located in the region out of the above criterion to derive the YSA, signifying a positive temperature dependence of strengthening without a distinct temperature-dependent stress peak in their flow stress [4]. [24]. It is generally accepted that the core structure of the dislocations controls those deformation phenomena that cannot be ascribed to long-range interactions between dislocations and/or between.

Commented [WW9]: 这些值的来源需要说明

Commented [WW10]: 句子没写完?

4.2 Deformation mechanisms transit from APB- to SISF-splitting at high temperatures

Unlike the straight screw dislocations often observed due to cube cross-slip, dislocation structures in the anomalous temperature region for $L1_2$ compounds exhibiting YSA at intermediate temperatures display different behavior. As mentioned above, the transmission of the crystallographic defects from the APBs at both 700 and 800 °C to the SISFs and nano twins at 900 °C can be found in the present CCIMA. The CCIMA features a similar dislocation dissociation behavior in the single crystal CMSX-4 superalloy, where superlattice stacking fault formation and twinning in superalloy are formed at high temperatures [52].

The type of dissociation for superlattice dislocations (APB-splitting SISF-splitting) depends on the stability of APB and the relative magnitude of APB and SISF energies. The

relative stability of the APB, CSF, and SISF has an important influence on the character of dislocation dissociation on {111} planes. This suggests that the increase in temperature may lead to the transition of dissociationscheme for the $[\bar{1}01]$ dislocation from APB-type to the SISF-type, despite that the formation energies for both SISF and APB decreases gradually with the temperature [53]. In other words, the increase in temperature would significantly decrease the SISF formation energy in the CCIMA, thereby enhancing the SISF and nano twinning. The energy criterion for the formation of SISF dislocations from elasticity calculation can be given with the following inequality [54]:

$$ln\left(\frac{8\pi\gamma_{SISF}}{a \cdot c_{44}}\right) < 2\,ln\left(\frac{4\pi\gamma_{APB}}{a \cdot c_{44}}\right) + 1\lambda \qquad (6)$$

where γ_{SISF} and γ_{APB} are the SISF and APB formationenergies on the (111) plane, respectively. a and c_{44} stand for the lattice constant and elastic constant, respectively. Based on the critical line referred from Paidar, the SISF dissociation is preferred only when the energy for SISF on the (111) plane is sufficiently low compared to APB [24]. Inspired by the critical line proposed by Paidar, the SISFE would decrease to 26.1 mJ/m^2 when deformed at 900 °C. In the meantime, the imposed stress on the twin partial dislocation should be higher than the energy threshold for twin partial formation i.e., $\sigma_{tw} > \gamma_{SISF}/(bm_{twin})$, which can be assumed as two adjacent SISF by which the nanotwin occurs [55]. By using an average Schmid factor of 0.326 for the FCC polycrystalline, the corresponding maximum critical axial stress needed to dissociate the dislocations can be estimated to be about ~ 549 MPa, which is lower than the actual true stress imposed on the CCIMA when deformed at 900 °C. Thus, SISF and nanotwin occur.

The APB-type dissociation can occur on both the (111) and the (010) planes while the

SISF only occurred on the (111) plane, so the dissociation of SISFs on the (111) plane makes the cross-slip from (111) to (010) irrelevant. In summary, the disappearance of the cross-slip segment and the formation of the SISFs or nanotwin responses for the decreased yield strength. Similarly, the absence of the anomalous temperature dependence of CRSS at high temperatures for slip on (111) in Pt_3Al has been interpreted in terms of the occurrence of the SISF-type dissociation for the [101] dislocation gliding on the (111) plane [23]. In addition, at the high temperature the grain boundary slip takes a leading role in carrying the deformation, which produces relatively low hardening in the alloy. Collectively, the deformation mechanism transition and correlated mechanical behavior of this alloy was further discussed based on the defect analysis, the temperature dependence of flow stress at 900 °C is responsible for the motion of superlattice dislocations with the SISF-splitting. Therefore, the disappearance of the anomalous temperature dependence of yield strength in the octahedral slip of this $L1_2$ alloy was caused by SISF coupled dissociation at 900 °C.

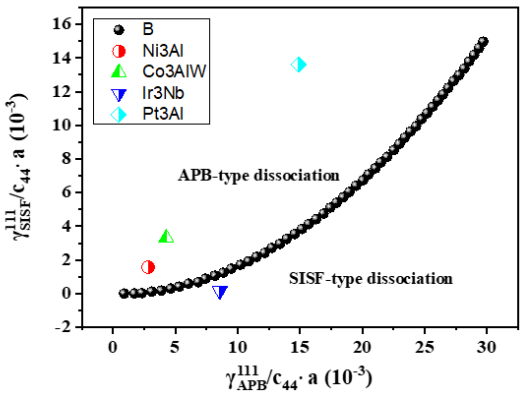

Fig. 11 Boundary map for APB- and SISF-type dissociation schemes of a parent [101]

dislocation in $L1_2$ compounds.

5. Conclusion

The present CCIMA contains the multi-component $(Ni, Co)_3(Al, Ti, Nb, Mo, Ta)$-type $L1_2$ phase, $(Ta, Nb, Mo)(Co, Ni)_2B$-type borides, together with the (Ni, Cr, Co)-rich FCC phase. An exceptional work-hardening rate of ~ 4530 ± 10 MPa without loss until failure is found at room temperature. It is superlattice dislocations separated by APB that dominate the deformation at a low strain, the presence of SISFs occurs with the strain at room temperature. A remarkable temperature-dependent anomaly in yield strength at a temperature below ~800 ℃ is formed, achieving a high strength of 957 MPa along with a strength increment by nearly 200 MPa relative to yield strength at 20 ℃. Thermally activated cross-slip of these APB-coupled dislocations from the octahedral (111) to cube (010) plane is responsible for the YSA. The transition of the dissociation scheme from APB-type at intermediate temperatures to SISF-type at high temperatures is believed to be responsible for the absence of YSA at 900 ℃. The designed CCIMA exhibits excellent mechanical properties for high-temperature structural applications.

Acknowledgment

The authors greatly acknowledge the financial support from the National Natural Science Foundation of China (Grant No. 52301174 and 52222112), All the authors declare that they have no known competing financial interests or personal relationships that could have appeared to influence the work reported in this paper.

Reference

[1] M. Yamaguchi, Y. Umakoshi, The deformation behaviour of intermetallic superlattice compounds, Progress in Materials Science 34(1) (1990) 1-148.

[2] A.I. Taub, R.L. Fleischer, Intermetallic Compounds for High-Temperature Structural Use, Science 243(4891) (1989) 616-621.

[3] H.A. Lipsitt, D. Shechtman, R.E. Schafrik, The deformation and fracture of Ti3Al at elevated temperatures, Metallurgical Transactions A 11(8) (1980) 1369-1375.

[4] D.-M. Wee, O. Noguchi, Y. Oya, T. Suzuki, New Ll2 ordered alloys having the positive temperature dependence of strength, Transactions of the Japan Institute of Metals 21(4) (1980) 237-247.

[5] V. Paidar, D.P. Pope, V. Vitek, A theory of the anomalous yield behavior in L12 ordered alloys, Acta Metallurgica 32(3) (1984) 435-448.

[6] K. Aoki, O. Izumi, Improvement in Room Temperature Ductility of the Intermetallic Compound Ni3Al by Ternary Trace Element Addition, Journal of the Japan Institute of Metals 43(4) (1979) 358-359.

[7] C.T. Liu, J.O. Stiegler, Ductile Ordered Intermetallic Alloys, Science 226(4675) (1984) 636-642.

[8] T. Yang, Y.L. Zhao, W.P. Li, C.Y. Yu, J.H. Luan, D.Y. Lin, L. Fan, Z.B. Jiao, W.H. Liu, X.J. Liu, J.J. Kai, J.C. Huang, C.T. Liu, Ultrahigh-strength and ductile superlattice alloys with nanoscale disordered interfaces, Science 369(6502) (2020) 427-432.

[9] K. Aoki, O. Izumi, 3pn. Inst, Met 43 (1979) 1190.

[10] Y.L. Zhao, W.C. Xiao, Z.K. Zhao, Q. Li, J. Cui, J.H. Luan, C.T. Liu, P.K. Liaw, T. Yang, A Co-rich chemically complex intermetallic alloy with extraordinary strength-ductility synergy, Scripta Materialia 229 (2023) 115371.

[11] B. Xiao, J. Zhang, S. Liu, Y. Zhao, L. Xu, C.T. Liu, T. Yang, Off-stoichiometry-guided design of high-strength chemically complex intermetallic-based alloys with outstanding ductility, Journal of Materials Science & Technology 160 (2023) 28-33.

[12] F.R. Long, S.I. Baik, D.W. Chung, F. Xue, E.A. Lass, D.N. Seidman, D.C. Dunand, Microstructure and creep performance of a multicomponent Co-based L12–ordered intermetallic alloy, Acta Materialia 196 (2020) 396-408.

[13] J. Hou, J. Gan, W. Li, H. Tian, X. Luo, J. Ju, Y. Zhou, S. Liu, H. Yao, Z. Chen, T. Yang, Exceptional high-temperature oxidation resistance and mechanisms of a novel chemically complex intermetallic alloy, Corrosion Science 225 (2023) 111607.

[14] S. Ochial, Y. Oya, T. Suzuki, Alloying behaviour of Ni3Al, Ni3Ga, Ni3Si and Ni3Ge, Acta Metallurgica 32(2) (1984) 289-298.

[15] D. Coutsouradis, A. Davin, M. Lamberigts, Cobalt-based superalloys for applications in gas turbines, Materials Science and Engineering 88 (1987) 11-19.

[16] Ş. Talaş, Nickel aluminides, Intermetallic Matrix Composites, Elsevier2018, pp. 37-69.

[17] K. Kumar, R. Sankarasubramanian, U.V. Waghmare, Tuning planar fault energies of Ni3Al with substitutional alloying: First-principles description for guiding rational alloy design, Scripta Materialia 142 (2018) 74-78.

[18] P.H. Thornton, R.G. Davies, T.L. Johnston, The temperature dependence of the flow stress of the γ′ phase based upon Ni3Al, 1(1) (1970) 207-218.

[19] V. Vitek, D.P. Pope, J.L. Bassani, Chapter 51 Anomalous yield behaviour of compounds with Ll2 structure, in: F.R.N. Nabarro, M.S. Duesbery (Eds.), Dislocations in Solids, Elsevier1996, pp. 135-185.
[20] V. Vitek, V. Paidar, Chapter 87 - Non-planar Dislocation Cores: A Ubiquitous Phenomenon Affecting Mechanical Properties of Crystalline Materials, in: J.P. Hirth (Ed.), Dislocations in Solids, Elsevier2008, pp. 439-514.
[21] J.B. Liu, D.D. Johnson, A.V. Smirnov, Predicting yield-stress anomalies in L12 alloys: Ni3Ge–Fe3Ge pseudo-binaries, Acta Materialia 53(13) (2005) 3601-3612.
[22] E.M. Schulson, J.A. Roy, The yield strength of the L12 phase Zr3Al, Acta Metallurgica 26(1) (1978) 29-38.
[23] N.L. Okamoto, Y. Hasegawa, W. Hashimoto, H. Inui, Plastic deformation of single crystals of Pt3Al with the L12 structure, Philosophical Magazine 93(1-3) (2013) 60-81.
[24] N.L. Okamoto, S. Takemoto, Z.M.T. Chen, M. Yamaguchi, H. Inui, FCC metal-like deformation behaviour of Ir3Nb with the L12 structure, International Journal of Plasticity 97 (2017) 145-158.
[25] Y. Yamabe-Mitarai, M.H. Hong, Y. Ro, H. Harada, Temperature dependence of the flow stress in Ir3Nb with the L12 structure, Philosophical Magazine Letters 79(9) (1999) 673-682.
[26] A.E. Vidoz, L.M. Brown, On work-hardening in ordered alloys, The Philosophical Magazine: A Journal of Theoretical Experimental and Applied Physics 7(79) (1962) 1167-1175.
[27] J.X. Hou, S.F. Liu, B.X. Cao, J.H. Luan, Y.L. Zhao, Z. Chen, Q. Zhang, X.J. Liu, C.T. Liu, J.J. Kai, T. Yang, Designing nanoparticles-strengthened high-entropy alloys with simultaneously enhanced strength-ductility synergy at both room and elevated temperatures, Acta Materialia (2022) 118216.
[28] Dang-Moon, Wee, Tomoo, Suzuki, The Temperature Dependence of Hardness of L12 Ordered Alloys, Transactions of the Japan Institute of Metals (1979).
[29] Y. Oya-Seimiya, T. Shinoda, T. Suzuki, Low temperature strength anomaly of L12 type intermetallic compounds Co3Ti and Pt3Al, Materials Transactions, JIM 37(9) (1996) 1464-1470.
[30] J.-W. Lee, S.-K. Hyun, M.-S. Kim, M.-G. Kim, T. Ide, H. Nakajima, Elevated temperature compression behaviors of lotus-type porous NiAl, Intermetallics 29 (2012) 27-34.
[31] K. Hagihara, H. Fujimoto, T. Nakano, Y. Umakoshi, Plastic deformation behavior of Ni3(Ti0.7Nb0.3) single crystals with D019 structure, Intermetallics 18(4) (2010) 434-440.
[32] Y. Umakoshi, K. Hagihara, T. Nakano, Operative slip systems and anomalous strengthening in Ni3Nb single crystals with the D0a structure, Intermetallics 9(10) (2001) 955-961.
[33] G. Chen, Y. Peng, G. Zheng, Z. Qi, M. Wang, H. Yu, C. Dong, C.T. Liu, Polysynthetic twinned TiAl single crystals for high-temperature applications, Nature materials 15(8) (2016) 876-881.
[34] C. Li, M. Zhao, J.C. Li, Q. Jiang, B2 structure of high-entropy alloys with addition of Al, Journal of Applied Physics 104(11) (2008) 113504.
[35] M.H. Yoo, On the theory of anomalous yield behavior of Ni3Al - Effect of elastic anisotropy, Scripta Metallurgica 20(6) (1986) 915-920.
[36] I. Baker, B. Huang, E.M. Schulson, The effect of boron on the lattice properties of Ni3Al, Acta Metallurgica 36(3) (1988) 493-499.
[37] J.P. Hirth, J. Lothe, Theory of dislocations, (1982).
[38] Z. Chen, K. Kishida, H. Inui, M. Heilmaier, U. Glatzel, G. Eggeler, Improving the intermediate- and high-temperature strength of L12-Co3(Al,W) by Ni and Ta additions, Acta Materialia 238 (2022) 118224.

[39] N.L. Okamoto, T. Oohashi, H. Adachi, K. Kishida, H. Inui, P. Veyssière, Plastic deformation of polycrystals of Co3(Al,W) with the L12 structure, Philosophical Magazine 91(28) (2011) 3667-3684.
[40] Y. Gao, Y. Ru, Y. Gao, X. Xia, Z. Zhong, Z. Shi, R. Jia, B. Hu, H. Zhao, W. Zhao, Y. Pei, S. Li, S. Gong, Full-operating-temperature tensile mechanisms of [111] oriented single-crystal superalloy: New intermediate temperature toughening behavior against ductility losing, Journal of Materials Science & Technology 212 (2025) 207-222.
[41] A. Korner, H.P. Karnthaler, C. Hitzenberger, Transmission electron microscopy study of cross-slip and of Kear-Wilsdorf locks in L12 ordered Ni3Fe, Philosophical Magazine A 56(1) (1987) 73-88.
[42] B.H. Kear, G.R. Leverant, J.M. Oblak, AN ANALYSIS OF CREEP-INDUCED INTRINSIC/ EXTRINSIC FAULT PAIRS IN A PRECIPITATION HARDENED NICKEL-BASE ALLOY, ASM (Amer. Soc. Metals), Trans. Quart., 62: 639-50(Sept. 1969). (1969) Medium: X 2009-12-15.
[43] R.A. Mulford, D.P. Pope, The yield stress of Ni3(Al, W), Acta Metallurgica 21(10) (1973) 1375-1380.
[44] A.T. Paxton, Y.Q. Sun, The role of planar fault energy in the yield anomaly in L12 intermetallics, Philosophical Magazine A 78(1) (1998) 85-104.
[45] H.P. Karnthaler, E.T. Mühlbacher, C. Rentenberger, The influence of the fault energies on the anomalous mechanical behaviour of Ni3Al alloys, Acta Materialia 44(2) (1996) 547-560.
[46] H. Kear, H.G.F. Wilsdorf, Trans. Metall. Soc 224(328) (1962).
[47] M. Yamaguchi, V. Paidar, D.P. Pope, V. Vitek, Dissociation and core structure of 〈110〉 screw dislocations in L12 ordered alloys I. Core structure in an unstressed crystal, Philosophical Magazine A 45(5) (1982) 867-882.
[48] V. Paidar, M. Yamaguchi, D.P. Pope, V. Vitek, Dissociation and core structure of screw dislocations in L12 ordered alloys II. Effects of an applied shear stress, Philosophical Magazine A 45(5) (1982) 883-894.
[49] Georges, Saada, Patrick, Veyssiere, The dissociation of a screw superdislocation in the L1₂ structure, Philosophical Magazine A (1992).
[50] Y. Ru, H. Zhao, H. Zhang, X. Pan, W. Zhao, Y. Pei, S. Li, S. Gong, Design for anomalous yield in γ'-strengthening superalloys, Materials & Design 183 (2019) 108082.
[51] S.V. Prikhodko, H. Yang, A.J. Ardell, J.D. Carnes, D.G. Isaak, Temperature and composition dependence of the elastic constants of Ni3Al, Metallurgical and Materials Transactions A 30(9) (1999) 2403-2408.
[52] D.M. Knowles, Q.Z. Chen, Superlattice stacking fault formation and twinning during creep in γ/γ' single crystal superalloy CMSX-4, Materials Science and Engineering: A 340(1) (2003) 88-102.
[53] A. Breidi, J. Allen, A. Mottura, First-principles modeling of superlattice intrinsic stacking fault energies in Ni3Al based alloys, Acta Materialia 145 (2018) 97-108.
[54] V. Paidar, D.P. Pope, M. Yamaguchi, Structural stability and deformation behavior of L12 ordered alloys, Scripta Metallurgica 15(9) (1981) 1029-1031.
[55] G.B. Viswanathan, S. Karthikeyan, P.M. Sarosi, R.R. Unocic, M.J. Mills, Microtwinning during intermediate temperature creep of polycrystalline Ni-based superalloys: mechanisms and modelling, Philosophical Magazine 86(29-31) (2006) 4823-4840.